Journal of the Brazilian Society of Mechanical Sciences and Engineering (2019) 41:540
https://doi.org/10.1007/s40430-019-2037-8

TECHNICAL PAPER

Homogenisation of elastic properties in FDM components using microscale RVE numerical analysis

M. S. Anoop[1] · **P. Senthil**[1]

Received: 26 May 2019 / Accepted: 18 October 2019 / Published online: 5 November 2019

Abstract

Fused deposition modelling (FDM) is an additive manufacturing method having the potential to fabricate functional components. As the inherent nature of additive structures, the component stiffness depends on the build parameters such as layer height and raster orientation in addition to the filament material properties. Even on FDM prints with 100% infill density, voids are formed along the interface of rasters and contribute to the characteristics of the component. The primary role of the present work is to determine elastic characteristics such as Young's modulus, shear modulus and Poisson's ratio of FDM components and study the effect of build parameters. The void geometry identified from the cross-sectional morphology was used to create a microscale representative volume element (RVE) model capturing the characteristics of the FDM print. The elastic constants of the microscale model RVE were estimated by volume average method and homogenised over the entire structure. The study also investigated the influence of layer height on the elastic behaviour of FDM components in two different raster orientations of 0° and 0°/90°. Both the conditions exhibited directional characteristics and the elasticity constants approaches filament characteristics with decreases in the layer height. The modulus of elasticity was found maximum in the direction of raster orientation, whereas the elasticity modulus along vertical direction exhibited the lowest. The components with 0°–90° raster orientation exhibited transversely isotropic characteristics. Thus, the actual cross-sectional morphology-based microscale numerical analysis can effectively predict the directional attributes of FDM prints.

Keywords FDM · Microscale numerical analysis · Cross-sectional morphology · RVE homogenisation · Orthotropic property

1 Introduction

Among extrusion-based additive manufacturing, fused deposition modelling has gained importance as a low-cost and easy manufacturing technique. FDM also known as fused layer modelling (FLM) or fused filament fabrication (FFF) is the additive manufacturing technique in which thermoplastic polymer-based filament is melted and deposited with controlled nozzle movement to fabricate 3D components directly from CAD model. FDM received wide acceptance as it reduced the lead time from conceptual design to functional components [1]. In the design phase, the part needs to be modelled using CAD software in STL (stereolithography) format. The 3D model in STL format is then adapted for layered manufacturing using slicing software and generates the machine code for printing [2]. The slicing software generates machine codes for FDM printing by customising the parameters of filament extrusion, temperature settings for the nozzle and build plate, nozzle movements, etc. The code carries instructions for feeding filament to the nozzle, heating nozzle to a temperature above the melting point of the polymer, nozzle and build plate movements, etc. The 3D printer fabricates the component by executing the codes from the slicing software. The fused filament fabrication is achieved by simultaneous extrusion of fused polymer and nozzle or build plate movement as per the instructions depicted in the code.

The most popular thermoplastic polymers used in FDM are acrylonitrile butadiene styrene (ABS), polylactic acid (PLA), polycarbonate (PC), polyamide (PA), polymethyl methacrylate (PMMA), polyethylene (PE) and polypropylene (PP). High strength and thermal resistant materials such

Technical Editor: João Marciano Laredo dos Reis.

✉ P. Senthil
senthil@nitt.edu

[1] Department of Production Engineering, National Institute of Technology, Tiruchirappalli, India

as polyetherimide (PEI/ULTEM) [3] and polyether ether ketone (PEEK) find printability with high-temperature printers expand the applicability of FDM [3]. The properties of FDM print components can improve by composite filaments [4–6] in the form of polymer blends [7], polymer matrix composites, fibre reinforced composites and polymer–ceramic composites [8–11]. The introduction of more printable filaments has elaborated the application of FDM components in the field of automotive [12, 13], aerospace [14, 15], medical [16] and manufacturing [17–19]. FDM printable conductive polymers fascinated researchers towards the developments of multifunctional components as sensors [20], capacitors [21] and other electronic instrumentation components [22, 23].

The properties of FDM are mainly contributed by the filament material used for printing. But as this fabrication technique is based on the fused deposition of polymer filament, stiffness of components also depends on the extent of bond formed between adjacent raster. As various process parameters influence the extent of blending with adjacent rasters, the mechanical characteristics of the FDM components also depend upon the process parameters [24]. The effect of process parameters such as layer height, raster angle, raster width, build orientation, extrusion temperature, feed rate and air gap (percentage infill) on tensile, compressive, flexural and impact strength of components has been reported in the literature [25]. The previous study on FDM-printed ABS parts reported anisotropic behaviour [26, 27]. The studies considered the influence of various parameters such as raster orientation, air gap, bead width, temperature and colour of filament material on part strength of ABS components. Analytical models were developed to predict strength and stiffness based on raster orientation and perimeter lines (number of contours) [28]. Among the build parameters, the air gap and raster orientation were reported as the most significant influencing parameter [29, 30]. The effect of extrusion temperature and print speed was also found influential on part strength [31, 32]. FDM part of ABS plus reported a significant influence of build direction on the elastic response of flat and curved layer FDM parts [33].

The effect of building parameters on flexural strength was studied in FDM components printed with Ultem material [34]. The study compared the flexural strength with different build directions (horizontal and vertical) with 0°/90° and 45°/−45° raster orientations in different air gaps. The components printed in the vertical direction with 0°/90° raster orientation exhibited higher flexural strength [35]. The influence of layer height and printing temperature on impact strength was studied on FDM printed with polypropylene revealed maximum strength attainment with build conditions of lower layer height and higher printing temperature [36]. The influence of nozzle temperature on strength can be optimised for maximum performance. The effect of process parameters on FDM specimens printed with PLA in different directions, layer height and feed rate was studied [37]. A regression model was developed for predicting the tensile and flexural strength of the components printed with these parameters. The process parameters of raster angle, layer height and raster width influence the strength; and the cross-sectional morphology captures the influence of print parameters in the specimen [38–40]. All these studies emphasised the importance of determining the directional properties of FDM prints.

The layer-by-layer addition of material in FDM induces heterogeneity in material distribution and results in directional behaviour of the printed component. The strength and properties of the FDM parts are influenced by the level of inter- and intralayer bonding of rasters [34]. The interlayer bonding is due to the coalescence of the adjacent rasters as the line width of raster exceeds the infill line distance (lateral distance between adjacent rasters). The intralayer bonding is mainly attributed by layer height adopted in printing. The build parameters such as layer height, raster width, infill line distance, build temperature and print speed control the extent of blending between adjacent rasters and contribute to the directional behaviour of properties [36, 37]. The influence of temperature also contributes to the extent of coalescence between raster [41]. The level of bonding based on extrusion temperature and time was studied, and a mathematical model for representing bonding was developed. Based on the level of adhesion between the rasters, voids are formed in print, and void geometry depends on the build parameters [32]. The geometry and orientation of these voids determine the mechanical characteristics of the print. The influence of process parameters on mechanical characteristics is consolidated in Table 1.

The FDM components are reported as exhibiting orthotropic properties with nine independent constitutive elements. The orthotropic model properties of FDM components printed with ABS and PLA were studied using classical lamination theory (CLT) [42]. The in-plane stiffness and strength of FDM components were predicted with combined CLT and Tsai–Hill yield criteria. This approach lacks to address the influence of building parameters such as nozzle temperature, feed rate and the extent of overlap between rasters.

An approach for determining the elastic properties by a mesoscale geometry model through the solution of an integral formulation using Greens function and homogenised the features to the macro-scale component was demonstrated [43]. Orthotropic constitutive model of FDM prints using PC filament based on nozzle diameter, slice height and raster width was developed and found a good correlation with physical test [44]. An analytical model based on mesostructure of the transverse void density and filament properties was developed and used for the optimisation of FDM-printed functional structures using Stratasys ABS P400 filament [45]. The stiffness and strength of FDM components depend on the shape and size of the voids

Table 1 Influence of process parameters on FDM mechanical characteristics

Characteristics	Material	Build parameter	Inferences	
Tensile strength Elasticity modulus	ABS	Raster angle Coalescence factor	Considering plane stress approach, analytical models are developed for determining elastic characteristics	[24]
Tensile strength Compressive strength	ABS	Air gap (0 and 0.0508) mm Road width (0.0508 and 1) mm Model temperature (270 and 280) °C ABS colour (blue and white) Orientation of raster (transverse and axial)	Reported air gap and raster orientation exhibit more significant influence on strength than other factors	[25]
Tensile strength Flexural strength Impact strength	ABS	Layer thickness (0.127, 0.178 and 0.254) mm Build orientation (0, 15 and 30)° Raster angle (0, 30 and 60)° Raster width (0.4064, 0.4564 and 0.5064) mm	Strength improves with smaller layer height, small raster angles and thick raster width	[26]
Tensile strength Elasticity modulus	ABS	Build orientation and contour lines (along thickness with 1, 4, 7 and 10 contours)	Increase in number of contour lines improves the tensile strength and stiffness for the specified raster orientation	[27]
Tensile strength Flexural strength Impact strength	ABS	Raster angle (0/−90, 18/−75, 30/−60 and 45/−45)° Raster gap (−0.05 and 0.05) mm	Raster angle +45/−45° exhibited maximum tensile and impact strength. 0°/90° exhibited maximum flexural strength	[28]
Tensile strength Fatigue strength	ABS	Raster angle (0, +45/−45, 45, and 90)°	Raster angle induced anisotropy. 0° raster orientation exhibits maximum ultimate and tensile strength	[29]
Tensile strength	ABS	Extruder temperature (230 and 270) °C Print speed (10 and 50) mm/s Layer height (0.1 and 0.3) mm Orientation (flat and vertical)	Tensile strength increases with decrease in speed and increase in extrusion temperature. Larger layer height in flat orientation and small layer height are recommended for vertical orientation	[30]
Flexural strength	PEI	Build direction (horizontal and vertical) Raster angle (0/90 and 45/−45)° Air gap: solid build (−0.00635, −0.0127 and −0.01905) mm Sparse build (2.54) mm	Solid build specimens exhibited higher flexural strength. Specimen built in vertical build direction and raster orientation 0/90 displayed higher strength	[34]
Tensile strength Elasticity modulus	PEI	Nozzle temperature (350, 360, 370 and 380) °C Orientation (0, 45, 90, ±45 and 0/90)° Layer thickness (0.15 and 0.2) mm Print speed (30 and 40) mm/s	The nozzle temperature can be optimised for maximum strength. Raster direction induces anisotropy in the component	[35]
Impact strength	PP	Layer height (0.1 and 0.3) mm Extrusion temperature (200 and 250) °C	Smaller layer height with higher temperature gives better impact strength	[36]
Tensile strength Flexural strength	PLA	Build orientation (flat, on-edge, upright) Layer thickness (0.06, 0.12, 0.18, 0.24) mm Feed rate (20, 50 and 80) mm/s	On-edge orientation met optimum performance in terms of strength and stiffness. High feed rate and lower layer thickness derive optimal performance	[37]
Tensile strength	PLA	Raster angle (0, 30, 45, 60 and 90)° Layer height (0.1, 0.15, 0.2, 0.25 and 0.3) mm Raster width (0.4, 0.5, 0.6 and 0.7) mm	Lower layer height with wider raster width and 0° raster angle exhibits better strength	[38]
Tensile strength	PLA	Layer thickness (0.1, 0.12, 0.15, 0.18 and 0.2) mm Infill orientation (0,18, 45, 72 and 90)° Number of shell perimeters (2, 3, 4, 5 and 6)	Modulus of elasticity and tensile strength are significantly influenced by layer height and infill orientations	[39]
Tensile strength	PLA and ABS	Pattern orientation (0/90 and +45/−45)° Layer height (0.2, 0.3 and 0.4) mm	Modulus of elasticity and tensile strength are significantly influenced by layer height and pattern orientations	[40]

[46]. Such mesoscale characteristics depend on the deposition strategies adopted in printing.

The porosity-dependent characteristics of FDM components can be studied by acquiring images of cross section and analysing corresponding finite element model. The effect of porosity was studied on FDM print with ABS material [47]. Porosity was determined using X-ray tomography for different orientations, and the engineering constants were estimated using finite element computation. This methodology involves excessive computation to determine the structure characteristics accurately. The constitutive model of FDM components can be estimated from the microscale RVE capturing the features of the print and homogenised over the entire region. RVE is the microscale

model of the repetitive unit in the component volume with its general material characteristics. The concept of homogenisation using numerical RVE was compared with the strength of material approach [48]. The homogenisation method was found suitable for predicting the behaviour of FDM components. An ABAQUS CAE-based plug-in 'Easy PBC' was developed for determining the elastic properties of RVE [49]. The plug-in identifies the geometry and applies the necessary boundary displacement for estimating the homogenised elastic properties based on the periodic boundary condition. The equivalent properties of the model were estimated by extracting reaction forces on the effective surface on which the displacement was applied. The proposed tool was efficient in determining the effective elastic properties of composite material RVE.

A multiscale approach was proposed for determining the mechanical characteristics of unidirectional FDM components [50]. The study involved a microscale analysis of the print with different layer heights and homogenised the virtues of RVE to the component. The constitutive material model of 3D printed structures was developed using RVE numerical homogenisation [51]. The study focused on properties of FDM 3D prints in horizontal and vertical orientations. RVE of horizontal plates was modelled along a layer for constitutive matrix development, whereas, for vertical plates, RVE-combining raster portions of three adjacent layers were employed for calculating constitutive matrix. The study proposed laminate model analysis for prints in the horizontal plane and orthotropic modelling for prints in the vertical plane.

The literature pointed to the build parameters dependence on the mechanical characteristics of FDM prints. Among the build parameters, layer height and raster orientation were projected as the most influential parameters for components with 100 percentage infill. The previous literature also brought the concept of homogenisation in studying the effect of layer height and extruded raster width on stiffness and failure limits of FDM prints. These studies were based on numerical analysis on the approximated RVE model, assuming a uniform percentage of overlap between adjacent rasters. The actual void formation differs from the approximation of uniform overlap of rasters. The real void geometry in component cross section depends on the build parameters, and it can be determined by examining the cross-sectional morphology. Thus, the impact of actual geometry necessitates the importance of identifying the elastic properties. These elastic properties can be used for predicting behaviour while designing functional components.

The present work aims to study the dependence of build parameters on elastic characteristics of the solid (100%) infill FDM components. Specifically, this study aims to estimate the effective properties of FDM components by numerical analysis of microscale RVE model representing actual cross-sectional morphology. The research also focuses on investigating the effect of layer height and raster orientation on FDM components based on the homogenisation of effective properties. Elastic constants of RVE are estimated using the volume average method by applying periodic boundary conditions for three linear strains and three shear strains. PLA filament was chosen as print material in the study, as it is widely used FDM material. The effective properties of microscale model estimated were confirmed with Easy PBC homogenisation plug-in in ABAQUS platform. Homogenised effective elastic properties of the FDM print were also verified by conducting the tensile test.

2 Numerical analysis and validation

2.1 Computational homogenisation

As FDM components are manufactured layer-by-layer addition of fused thermoplastic polymer, it exhibits orthotropic characteristics. So, the constitutive relation of FDM prints follows the orthotropic material model. The directional conventions followed in this work are shown in Fig. 1. The direction of raster orientation is followed as axis 1, transverse to raster direction as axis 2 and vertical direction as axis 3.

The generalised Hook's law was used for the estimation of effective properties of microscale RVE. The stress–strain relation in the orthotropic model is expressed as:

$$\begin{bmatrix} \bar{\sigma}_{11} \\ \bar{\sigma}_{22} \\ \bar{\sigma}_{33} \\ \bar{\sigma}_{12} \\ \bar{\sigma}_{13} \\ \bar{\sigma}_{23} \end{bmatrix} = \begin{bmatrix} C_{11} & C_{12} & C_{13} & 0 & 0 & 0 \\ C_{12} & C_{22} & C_{23} & 0 & 0 & 0 \\ C_{13} & C_{23} & C_{33} & 0 & 0 & 0 \\ 0 & 0 & 0 & C_{44} & 0 & 0 \\ 0 & 0 & 0 & 0 & C_{55} & 0 \\ 0 & 0 & 0 & 0 & 0 & C_{66} \end{bmatrix} \begin{bmatrix} \bar{\varepsilon}_{11} \\ \bar{\varepsilon}_{22} \\ \bar{\varepsilon}_{33} \\ \bar{\gamma}_{12} \\ \bar{\gamma}_{13} \\ \bar{\gamma}_{23} \end{bmatrix} \tag{1}$$

where $\bar{\sigma}_{ij}$ and $\bar{\varepsilon}_{ij}$, $\bar{\gamma}_{ij}$ are average stress and strain tensor computed over the volume of the RVE and C_{ij} are the elements of the stiffness matrix.

The strain–displacement relation takes the form:

$$\begin{aligned} \bar{\varepsilon}_{11} &= \frac{\partial u_1}{\partial 1} \\ \bar{\varepsilon}_{22} &= \frac{\partial u_2}{\partial 2} \\ \bar{\varepsilon}_{33} &= \frac{\partial u_3}{\partial 3} \\ \bar{\gamma}_{12} &= \frac{\partial u_2}{\partial 1} + \frac{\partial u_1}{\partial 2} \\ \bar{\gamma}_{13} &= \frac{\partial u_3}{\partial 1} + \frac{\partial u_1}{\partial 3} \\ \bar{\gamma}_{23} &= \frac{\partial u_2}{\partial 3} + \frac{\partial u_3}{\partial 2} \end{aligned} \tag{2}$$

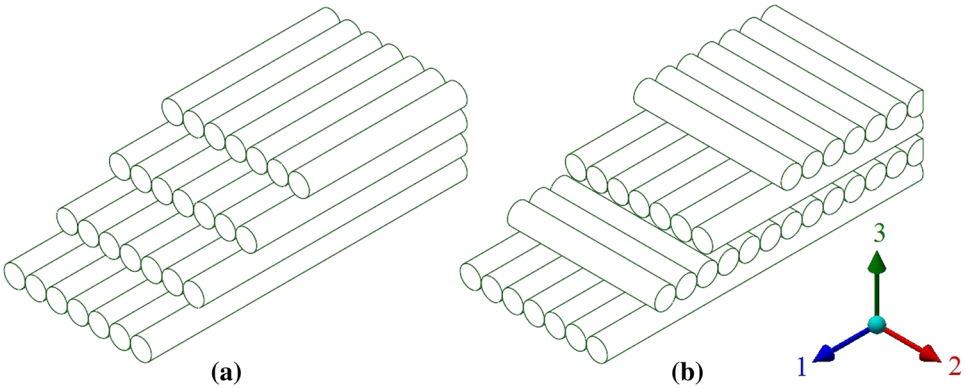

Fig. 1 Coordinate system: **a** rasters in 0° orientation and **b** rasters in 0°/90° orientation

where u_1, u_2 and u_3 are the displacements in the three orthogonal directions along axis 1, 2 and 3.

For determination of elastic constants, the RVE is applied with boundary conditions of each strain condition separately. By application of six independent strains and maintaining other strain values as zero, the effective constitutive elements can be evaluated by extracting the corresponding directional stress components developed in RVE, as shown in Eq. 3:

$$\bar{C}_{ij} = \frac{\text{Volume average of corresponding stress component in RVE}}{\text{Corresponding elementary strain applied in RVE}}$$
$$\text{i.e.,} \quad \bar{C}_{ij} = \frac{\bar{\sigma}_{ij}}{\varepsilon_{ij}} \tag{3}$$

$$\text{where} \quad \bar{\sigma}_{ij} = \frac{1}{V_{\text{RVE}}} \int_v \sigma_{ij} \mathrm{d}v. \tag{4}$$

All the constitutive elements can be determined by independently applying three linear and three shear strain conditions. The compliance matrix can be estimated by taking the inverse of the constitutive matrix. Engineering constants can be calculated from the compliance matrix element as per Eq. 5:

$$\begin{bmatrix} \bar{\varepsilon}_{11} \\ \bar{\varepsilon}_{22} \\ \bar{\varepsilon}_{33} \\ \bar{\gamma}_{12} \\ \bar{\gamma}_{13} \\ \bar{\gamma}_{23} \end{bmatrix} = \begin{bmatrix} 1/E_1 & -\nu_{21}/E_2 & -\nu_{31}/E_3 & 0 & 0 & 0 \\ -\nu_{12}/E_1 & 1/E_2 & -\nu_{32}/E_3 & 0 & 0 & 0 \\ -\nu_{13}/E_1 & -\nu_{23}/E_2 & 1/E_3 & 0 & 0 & 0 \\ 0 & 0 & 0 & 1/G_{12} & 0 & 0 \\ 0 & 0 & 0 & 0 & 1/G_{13} & 0 \\ 0 & 0 & 0 & 0 & 0 & 1/G_{23} \end{bmatrix} \begin{bmatrix} \bar{\sigma}_{11} \\ \bar{\sigma}_{22} \\ \bar{\sigma}_{33} \\ \bar{\sigma}_{12} \\ \bar{\sigma}_{13} \\ \bar{\sigma}_{23} \end{bmatrix} \tag{5}$$

where E_1, E_2 and E_3 are Young's moduli along with the first, second and third orientations, respectively; G_{12}, G_{13} and G_{23} are shear moduli, and ν_{12}, ν_{13} and ν_{23} are Poisson's ratios in the respective planes.

The effective orthotropic properties of the RVE can be calculated from the compliance matrix using Eq. 5. Elastic properties, thus determined by applying each linear and shear strains on the RVE model, capture the elastic characteristics of the FDM print in microscale. The raster angle effect can be obtained by transformation of the compliance matrix [52]. As the effect of raster angle is only in horizontal plane, the transformation is confined to that plane. The compliance matrix transform form is given by Eq. 6:

$$\left[S'\right] = \left[\bar{T}\right][S]\left[\bar{T}\right]^{\mathrm{T}} \tag{6}$$

where $[S']$ is the compliance matrix defined for new raster angle, $[S]$ is the compliance matrix in defined with original raster orientation as applied in the RVE, and $\left[\bar{T}\right]$ is the transformation matrix given in Eq. 7:

$$\left[\bar{T}\right] = \begin{bmatrix} l_1^2 & m_1^2 & n_1^2 & l_1m_1 & l_1n_1 & m_1n_1 \\ l_2^2 & m_2^2 & n_2^2 & l_2m_2 & l_2n_2 & m_2n_2 \\ l_3^2 & m_3^2 & n_3^2 & l_3m_3 & l_3n_3 & m_3n_3 \\ 2l_1l_2 & 2m_1m_2 & 2n_1n_2 & l_1m_2+l_2m_1 & l_1n_2+l_2n_1 & m_1n_2+m_2n_1 \\ 2l_1l_3 & 2m_1m_3 & 2n_1n_3 & l_1m_3+l_3m_1 & l_1n_3+l_3n_1 & m_1n_3+m_3n_1 \\ 2l_2l_3 & 2m_2m_3 & 2n_2n_3 & l_2m_3+l_3m_2 & l_2n_3+l_3n_2 & m_2n_3+m_3n_2 \end{bmatrix}$$
$$\begin{array}{lll} l_1 = \cos\theta & m_1 = \sin\theta & n_1 = 0 \\ l_2 = -\sin\theta & m_2 = \cos\theta & n_2 = 0 \\ l_3 = 0 & m_3 = 0 & n_3 = 1 \end{array} \tag{7}$$

where l, m and n are the direction cosines for transformation to a raster angle 'θ' from the principle RVE raster orientation as shown in Fig. 2.

These properties estimated in the microscale RVE are assumed homogeneous over the macro-scale FDM structure.

2.2 Cross-sectional morphology study

FDM samples were prepared for layer heights of 0.1, 0.2, 0.3 and 0.4 mm with two different infill raster orientation models of 0° and 0°/90° in alternate layers, as shown in Fig. 1. The filament used for printing was of 2.85 mm diameter PLA filament procured from 'WOL 3D'. The print parameters chosen for the study are depicted in Table 2.

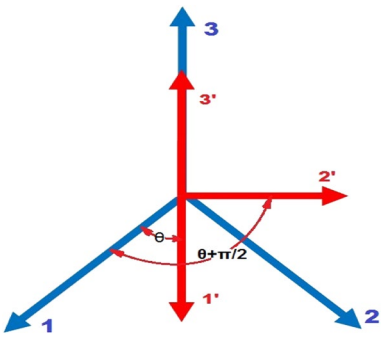

Fig. 2 Transformation of RVE orientation to raster angle. 1, 2 and 3 represent the RVE axes; 1′, 2′ and 3′ represent the transformations axes with raster angle θ degree in horizontal plane

Table 2 FDM build parameters

Parameter	Values	Units
Layer height	0.1, 0.2, 0.3, 0.4	mm
Raster width	0.44	mm
Infill line distance	0.4	mm
Nozzle diameter	0.4	mm
Printing temperature	190	°C
Build plate temperature	50	°C
Print speed	60	mm/s

The printed samples were fractured, and scanning electron microscopy (SEM) morphologies of the cross sections were captured after sputtering the sectioned surface. The SEM morphology of the cross sections was taken using VEGA3 TESCAN. The obtained cross-sectional morphology of FDM prints with 0.4 mm layer thickness in 0° and 0°/90° raster orientations is shown in Fig. 3. The cross-sectional morphology of the print samples exhibited an array of voids along each layer boundary. The void geometry based on the cross-sectional image was used for determining the microscale RVE geometry representing features of the entire volume.

2.3 Development of RVE model

The microscale RVE model resembling the cross section was created by identifying the periodic cells with a void along the layer and raster boundaries. The mean area of voids from actual cross-sectional morphology was determined by using an open-source image processing software 'ImageJ'. The SEM cross-sectional morphology was processed to isolate the voids by proper thresholding and measured the mean area of voids as shown in Fig. 4b. The three-dimensional RVE apprehending the actual shape and area of voids were modelled using 'ANSYS SpaceClaim Direct Modeler' software. Figure 4c represents the array of voids and the repetitive unit geometry in cross section. The RVE model for 0° and 0°/90° raster orientation is shown in Fig. 5.

2.4 Numerical analysis of RVE

The properties of RVE were determined by numerical analysis using FEA software ANSYS Workbench. The RVE model was assigned with property obtained from tensile testing of PLA filament procured from WOL 3D. The PLA filament was tested to obtain tensile characteristics. Filaments of length 150 mm with a gauge length of 100 mm were tested using Tinius Olsen H25KL with 25 kN load cell. The test was conducted with a crosshead speed of 1 mm/min. The properties of filament derived from the test are

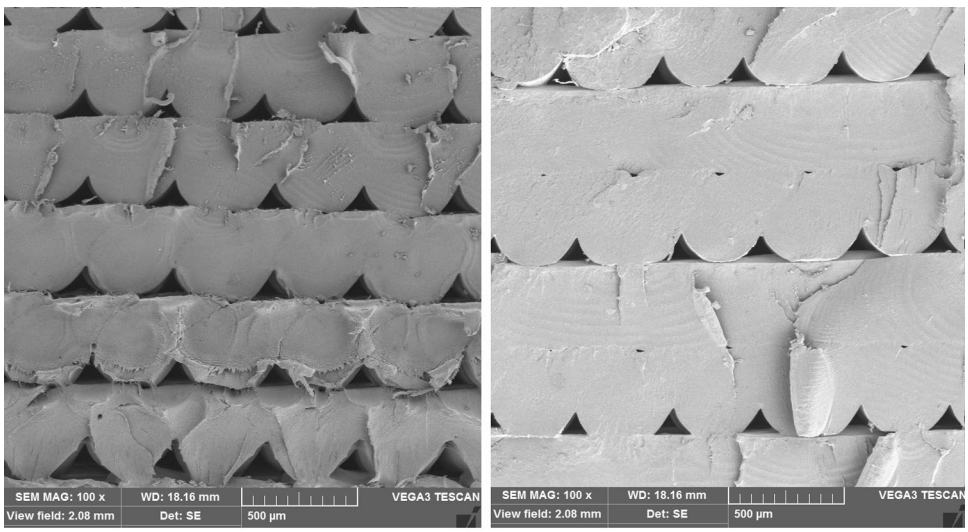

(a) **(b)**

Fig. 3 **a** SEM morphology of FDM print with 0° raster orientation and **b** 0°/90° raster orientation

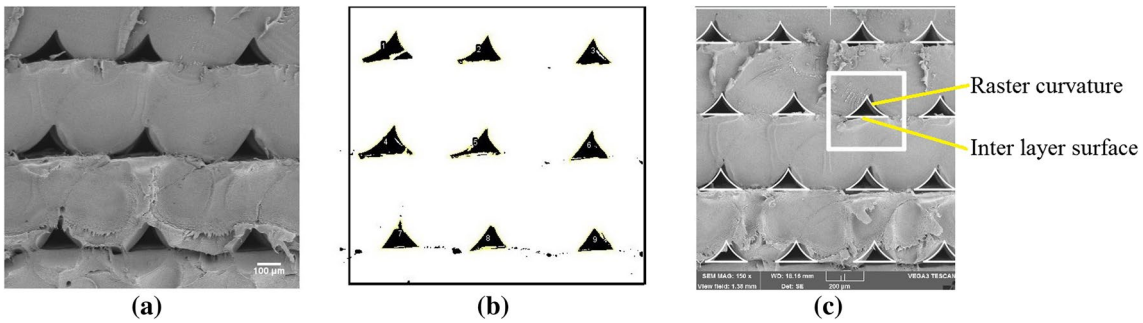

Fig. 4 **a** SEM morphology of RVE model, **b** voids indentified from the SEM using ImageJ and **c** the RVE cross section mapped with array of voids created using average of void area

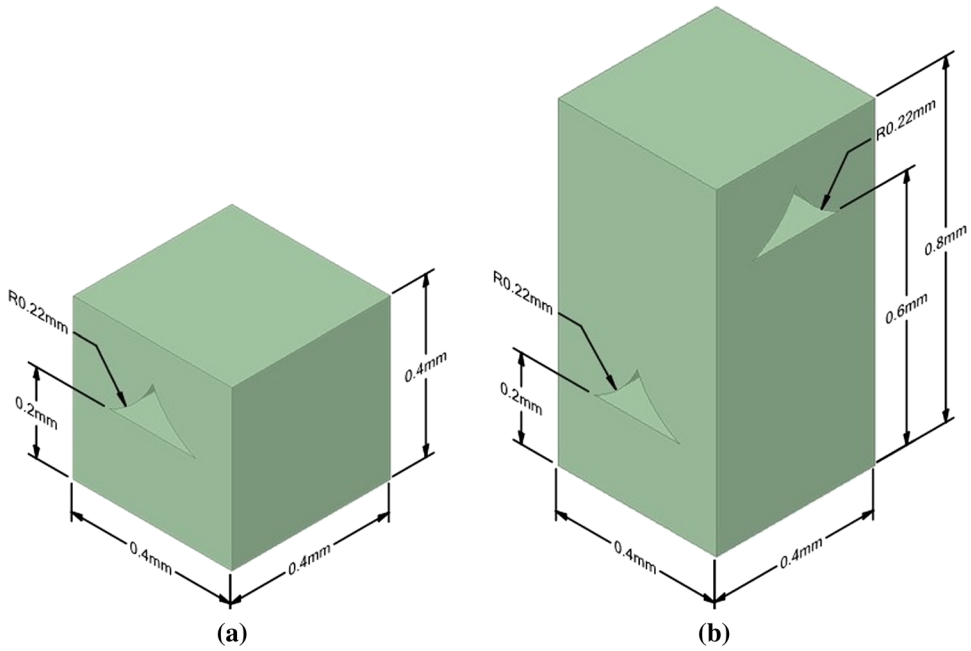

Fig. 5 RVE model developed for **a** 0° and **b** 0°/90° raster orientations

Table 3 Properties of PLA filament

Material properties	Value	Units
Young's modulus (E)	3370	MPa
Yield stress (σ_y)	30	MPa
Yield strain (ε_y) (elongation at yield)	1.93	%
Ultimate stress (σ_u)	36	MPa
Breaking strain (ε_b) (elongation at break)	11.1	%

shown in Table 3 and were used for the numerical analysis. For applying the linear and shear strain, six separate boundary conditions were applied on the RVE. Figure 6 shows a virtual RVE model, and Fig. 7 shows the deformation on enforcing six independent strain conditions. The independent strain conditions were achieved by applying the separate displacements as detailed in Table 4, on a virtual RVE with boundary surfaces $A1$–$A2$ separated by a distance 'a' along

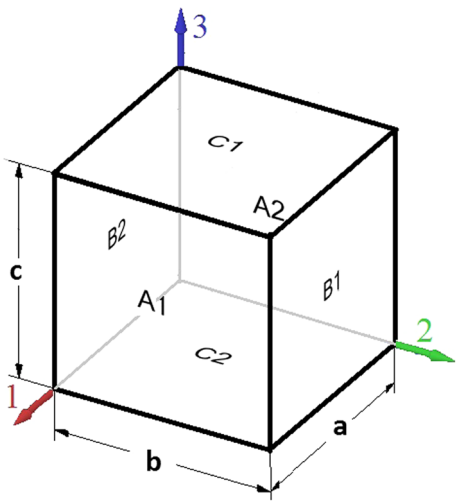

Fig. 6 Virtual RVE model showing orientation and boundary surfaces

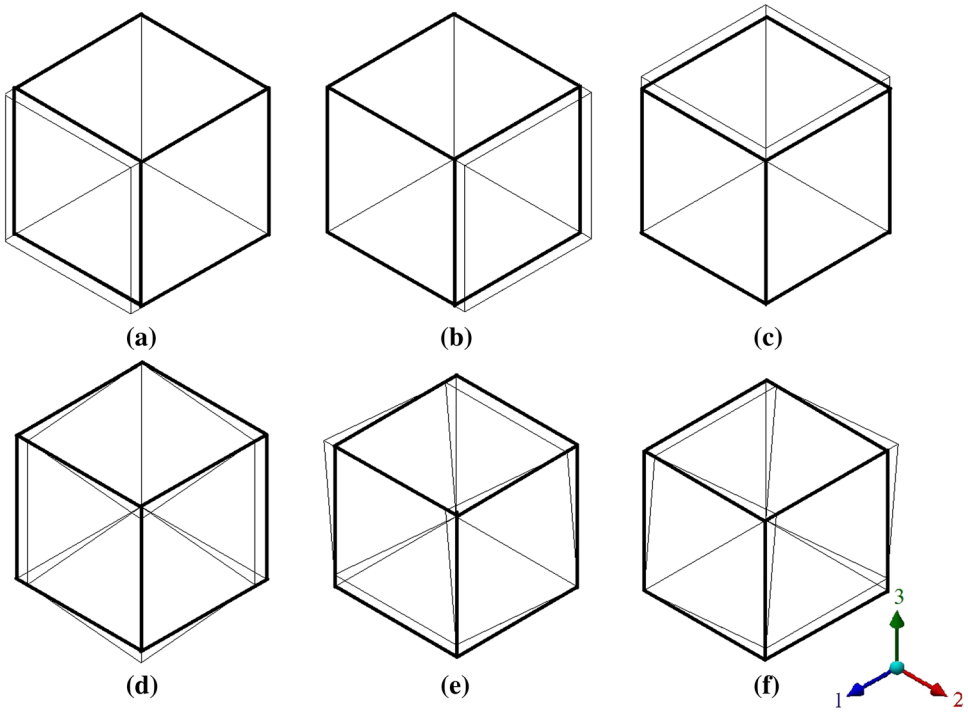

Fig. 7 Deformations on virtual RVE model on six independent strain boundary conditions

Table 4 Displacement boundary conditions for an RVE with dimensions a, b and c

Strain	Displacements	Surface					
		A_1	A_2	B_1	B_2	C_1	C_2
$\varepsilon_{11}=0.01$	u_1	$a\times0.01$	0	Free	Free	Free	Free
	u_2	Free	Free	0	0	Free	Free
	u_3	Free	Free	Free	Free	0	0
$\varepsilon_{22}=0.01$	u_1	0	0	Free	Free	Free	Free
	u_2	Free	Free	$b\times0.01$	0	Free	Free
	u_3	Free	Free	Free	Free	0	0
$\varepsilon_{33}=0.01$	u_1	0	0	Free	Free	Free	Free
	u_2	Free	Free	0	0	Free	Free
	u_3	Free	Free	Free	Free	$c\times0.01$	0
$\gamma_{12}=0.01$	u_1	$b\times0.005$	0	Free	Free	Free	Free
	u_2	Free	Free	$a\times0.005$	0	Free	Free
	u_3	Free	Free	Free	Free	0	0
$\gamma_{13}=0.01$	u_1	$c\times0.005$	0	Free	Free	Free	Free
	u_2	Free	Free	0	0	Free	Free
	u_3	Free	Free	Free	Free	$a\times0.005$	0
$\gamma_{23}=0.01$	u_1	0	0	Free	Free	Free	Free
	u_2	Free	Free	$c\times0.005$	0	Free	Free
	u_3	Free	Free	Free	Free	$b\times0.005$	0

axis 1; $B1$–$B2$ separated by distance 'b' along axis 2; and $C1$–$C2$ separated by a distance of 'c' along axis 3.

The RVE models were applied with the straining conditions, and the mesh size was refined along the corner edges of the void for obtaining convergence. The deformation plots observed on straining the RVE model of 0.4 mm layer thickness with 0° raster orientation are shown in Fig. 8. Using ANSYS APDL commands, elemental average stresses and

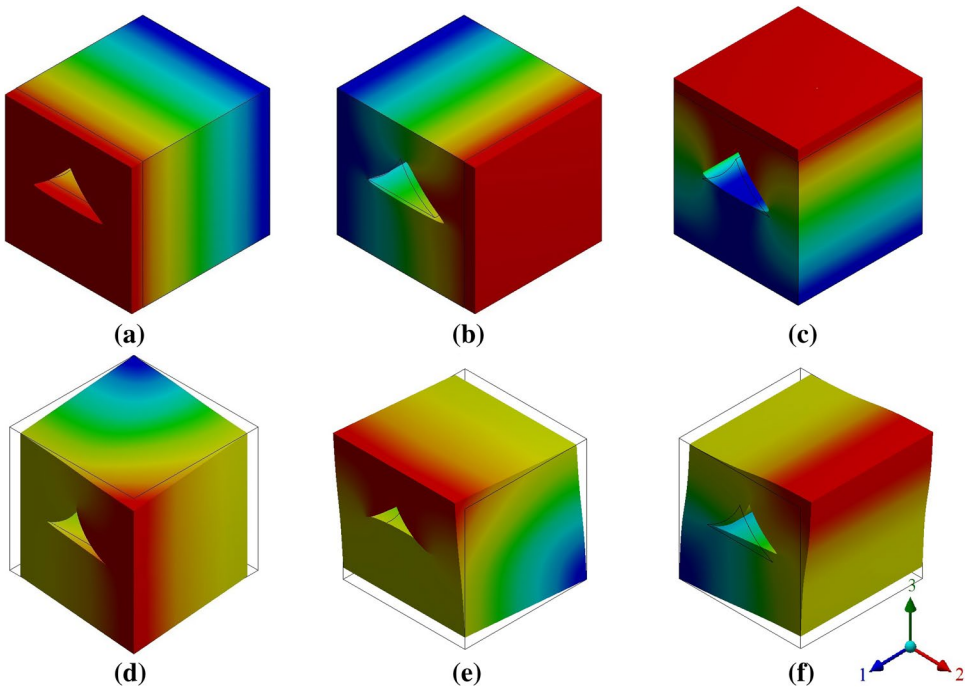

Fig. 8 Deformations on cross-sectional morphology-based RVE with six independent straining conditions

elemental volume were extracted. The volume average of stress was calculated by the cumulative elemental volume stress over the RVE volume. Similarly, volume averages of stresses in each strain condition were calculated. The constitutive matrix was estimated using volume average stresses and strains in RVE. The constitutive matrix computed for 0° and 0°/90° raster oriented RVE with 0.4 mm layer thickness was obtained as follows:

Constitutive matrix for FDM print 0° raster with 0.4 mm layer height:

$$C = \begin{bmatrix} 4537.9 & 2041.6 & 1723.8 & 0 & 0 & 0 \\ & 4048.4 & 1622.6 & 0 & 0 & 0 \\ & & 3165.8 & 0 & 0 & 0 \\ & & & 1087.6 & 0 & 0 \\ & \text{Symmetric} & & & 941.1 & 0 \\ & & & & & 970.4 \end{bmatrix} \text{MPa}$$

Constitutive matrix for FDM print 0°/90° raster with 0.4 mm layer height:

$$C = \begin{bmatrix} 4293.1 & 2043.1 & 1672.5 & 0 & 0 & 0 \\ & 4289.9 & 1676.2 & 0 & 0 & 0 \\ & & 3157.6 & 0 & 0 & 0 \\ & & & 1087.6 & 0 & 0 \\ & \text{Symmetric} & & & 955.9 & 0 \\ & & & & & 959.5 \end{bmatrix} \text{MPa}$$

The analysis was repeated for the RVE models with layer height 0.1, 0.2 and 0.3 mm in two orientations, and the elastic constants of RVE were determined using Eqs. 1–5.

2.5 Validation

2.5.1 Numerical validation

The results observed from the volume average method were verified with other numerical and experimental techniques. The results were verified with homogenised properties determined by numerical analysis of the RVE model using 'Easy PBC' plug-in within ABAQUS CAE platform. Easy PBC plug-in determines the properties based on the reaction forces acting on the effective surfaces area of the RVE while applying constrained strain.

2.5.2 Experimental testing

The experimental verification was done by conducting a tensile test using ASTM D 638 FDM specimen printed with build parameters adopted in morphology study. The software 'ANSYS Workbench' was used to model ASTM D 638 samples in STL format. The model was then processed using 'Ultimaker Cura 3.2' software for generating codes to fabricate tensile samples in three different orientations with build parameters as specified earlier in Table 2. The specimen for cross-sectional morphology study and tensile test were printed using 'Ultimaker 3 Extended'. The five tensile samples in each of the three different print orientations (1, 2 and 3rd) were fabricated in both 0° and 0°/90° raster orientations, as shown in Fig. 9. The specimen for determining elasticity modulus E_1 was fabricated such that its loading axis was along the direction 1. Similarly, the sample for determining E_2 and E_3 was fabricated with its loading directions

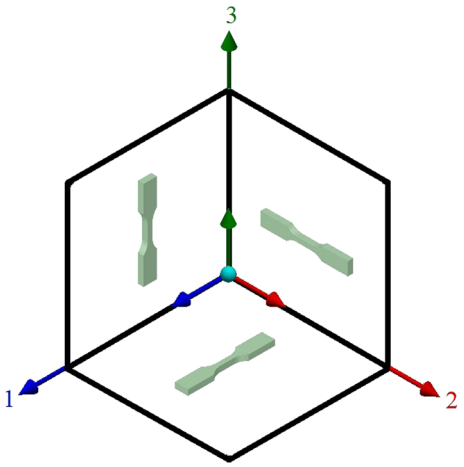

Fig. 9 Tensile specimens build orientation

along the respective axes. In all the print orientations, the raster angle was maintained same for both 0° and 0°/90° raster specimens. The linear elastic moduli were determined from the samples printed in three orientations. The tensile test was carried out on Tinius Olsen H25KL at a crosshead speed of 5 mm/min.

3 Results and discussion

3.1 Surface morphology of cross section

The cross section of FDM prints revealed the influence of print parameters on interlayer and intralayer adhesion. Cross-sectional morphology obtained from SEM image showed the extent of the actual adhesion between the rasters when printed with the build parameters as mentioned earlier. In each layer, the complete coalescence occurred only on the upper half region of layer thickness. The viscosity and rapid solidification of the fused filament restricted the perfect filling in the raster gap and left voids along the lower junction of rasters. In each layer, nozzle sweep on the layer surface created a flat top surface, and incomplete adhesion between rasters resulted in surface abnormalities along with the bottom layer interfaces. This anomaly is continued through the entire layers and resulted in a continuous array of voids in the layered structure. The voids thus generated resembled the shape of a triangle with a flat lower base and raster curvature instead of slant edges, as shown in Fig. 4. In 0° raster orientation, the voids were formed along each layer interface. The arrays of these voids in 0°/90° raster orientation were aligned mutually perpendicular along adjacent layer interfaces. The presence of these voids induces directional properties in the FDM components. As the layer height decreases, the extruded material gets squeezed, and void geometry shrinks.

3.2 Analysis of RVE

Microscale RVE for different layer heights was modelled based on the geometry of repeating array. The micromechanical study of the RVE was done in ANSYS Workbench for determining elastic constants by applying boundary conditions for six strains separately. On enforcing boundary conditions, the RVE gets strained, and elemental stresses were generated. The average stress on each element and elemental volume were extracted, and the total volume averages of stress components of RVE were calculated. The constitutive matrix of RVE was developed by using the volume average stress components and corresponding applied strain. Then, the properties of the RVE were determined as per Eqs. 1–5. Compliance matrix was obtained by taking the inverse of the constitutive matrix. The elastic constants were calculated from the compliance components.

Table 5 Comparison of present study with Easy PBC

Elastic constants	Numerical analysis					
	0° raster orientation			0°/90° raster orientation		
	Present study	Easy PBC	Percentage deviation (%)	Present study	Easy PBC	Percentage deviation (%)
E_1 (MPa)	3182.35	3179.25	0.10	3014.69	3007.11	0.25
E_2 (MPa)	2844.13	2845.66	−0.05	3008.39	3007.53	0.03
E_3 (MPa)	2281.74	2290.57	−0.39	2272.47	2261.68	0.47
G_{12} (MPa)	1087.6	1096.00	−0.77	1087.60	1094.82	−0.66
G_{13} (MPa)	941.14	959.30	−1.93	955.92	966.17	−1.07
G_{23} (MPa)	970.35	977.00	−0.69	959.45	966.17	−0.70
ν_{12}	0.32	0.32	0.00	0.34	0.338	0.31
ν_{13}	0.35	0.36	−2.86	0.35	0.35	−0.20
ν_{23}	0.33	0.34	−3.03	0.35	0.35	0.36

The proposed volume average method for evaluation of elastic constants is compared with properties derived from Easy PBC plug-in which is based on the boundary method for determining the equivalent stress. The elastic constant's value evaluated by applying the proposed scheme showed good correlation with results from Easy PBC plug-in. The comparison of present numerical study with Easy PBC is presented in Table 5.

The experimental test on five samples in each orientation were used to determine the mean elastic constants. The mean values of experimental tensile test results were considered for comparing with numerical results. Experimentation results exhibited lower values compared to the numerical analysis results. In 0° raster orientation specimen, the mean values of elastic constants obtained from tensile testing were 3015.25, 2659.05 and 2054.90 MPa with a standard deviation of +/− 110.13, +/− 120.21 and +/− 184.17 MPa, respectively, whereas for 0°/90° specimens, the test results were 2883.00, 2890.30 and 2045.10 MPa with standard deviations of +/− 114.52, +/− 112.18 and +/− 172.04 MPa, respectively. Results in vertically printed samples showed the maximum deviation of 10.01% among linear elastic constants. The comparison of numerical results with that of physical testing is shown in Table 6. The comparison of Young's modulus in the present study with the numerical Easy PBC results and experimental results is shown in Fig. 10.

All the elasticity moduli observed in experimentation were within the acceptable level with maximum percentage deviation of 10.1% compared to the microscale numerical analysis. In the proposed microscale model, the coalescence region is assumed perfect with continuous material distribution, and the edge effects of the rasters on the boundary of components were not considered. These might be the reason for the slight deviation from experimental results. The inclusion of minor cracks or cavities and the improper adhesion of the rasters beyond the scope of microscale RVE analysis might result in the lower performance in experimentation.

The effects of layer height were studied by the numerical analysis of RVE based on the cross-sectional geometry observed with the print conditions. By straining the RVE, the stress tensors were formed in RVE, and directional elastic properties were estimated based on the volume average method of homogenisation. The variations of elastic constants with layer height are shown in Figs. 11 and 12, for 0° and 0°/90° raster orientations, respectively. In all cases, the modulus of elasticity decreases with increase in layer height as the void size increases.

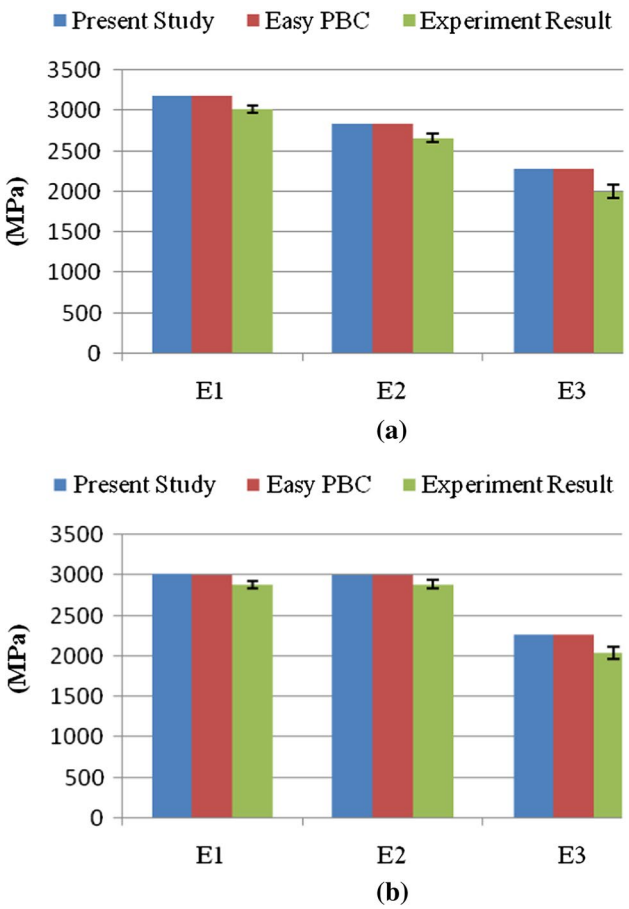

Fig. 10 Comparison of Young's moduli, **a** 0° raster oriented component; **b** 0°/90° raster oriented component

In 0° raster orientation, Young's modulus in the direction of raster orientation remained highest among all levels of layer heights. For determining Young's modulus in the transverse direction, the RVE is strained along the second axis. While straining in transverse raster direction,

Table 6 Comparison of present study and tensile test results for 0° and 0°/90° raster orientation

Young's modulus	0° raster orientation			0°/90° raster orientation		
	Present study	Tensile test Mean ± SD	Deviation %	Present study	Tensile test Mean ± SD	Deviation %
E_1 (MPa)	3182.35	3015.25 ± 110.13	5.25	3014.69	2883.00 ± 114.52	4.37
E_2 (MPa)	2844.13	2659.05 ± 120.21	6.51	3008.39	2890.30 ± 112.18	3.93
E_3 (MPa)	2281.74	2054.90 ± 184.17	9.94	2272.47	2045.10 ± 172.04	10.01

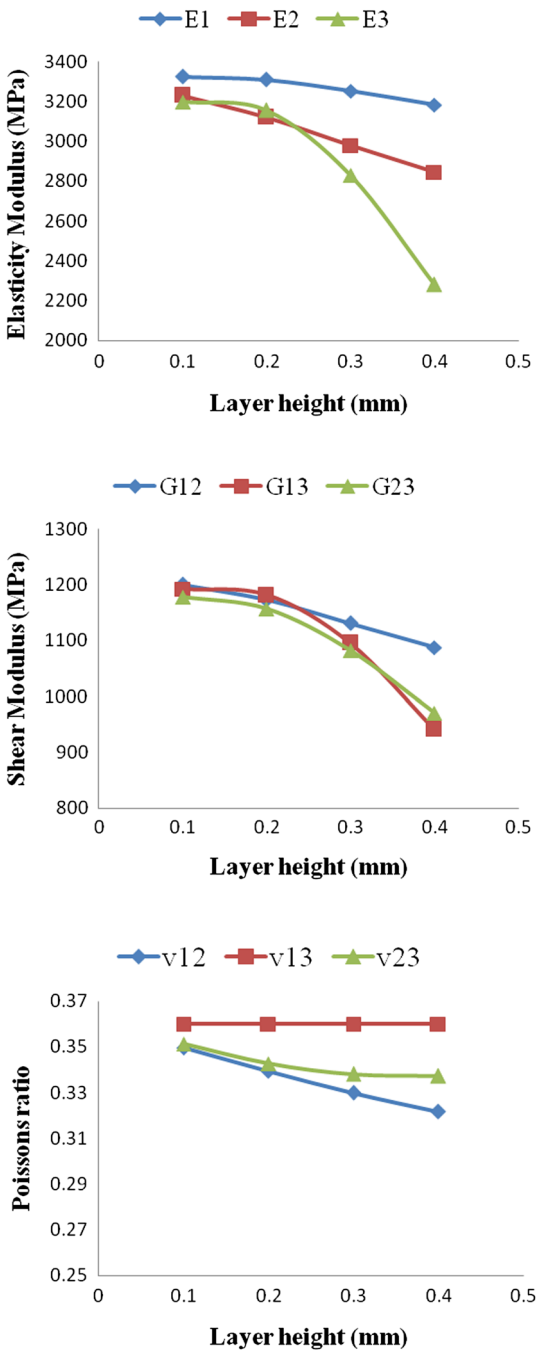

Fig. 11 Variation of elastic constants with layer height in 0° raster orientation

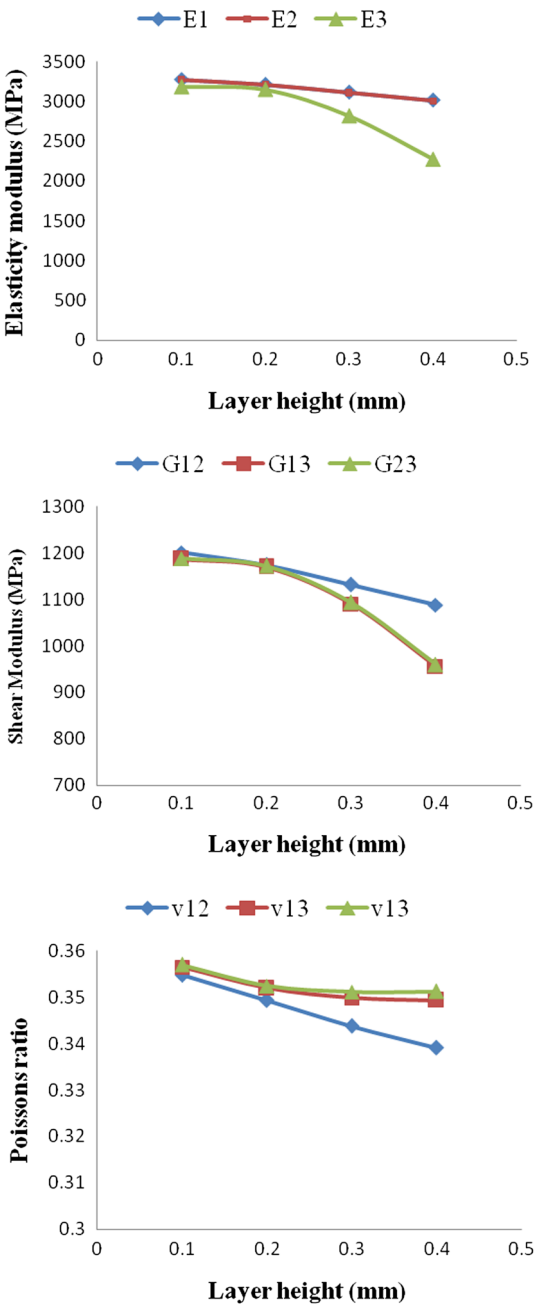

Fig. 12 Variation of elastic constants with layer height in 0°/90° raster orientation

the stress concentration occurs at the junction of raster curves at the top corner of the void and the presence of void reduces the area of load transfer. As the stress concentrates on a smaller region, the effective volume average stress is less compared to that in raster directional straining. Hence, the effective Young's modulus along the second axis is lower. Similarly, strain in the vertical direction causes the stress concentration at the corners of the lower edge of the voids resulting in the lowest magnitude of elasticity along the third axis. The shear modulus decreases along plane 12 with an increase in layer height as the void surface gets deformed on shear loading, but the shear modulus along the other two planes reduces further with an increase in layer height as the out of plane deformations are restricted by the boundary conditions for shear

stress on 13 and 23 planes. This print condition exhibited a reduction of Young's modulus by 28% along the third axis with the increase in layer height from 0.1 mm to 0.4 mm, whereas 4% to 12% reduction along the first and second axis, respectively. Similarly, shear modulus exhibited a reduction of 9%, 21% and 17% for G_{12}, G_{13} and G_{23}, respectively, as layer height increased from 0.1 mm to 0.4 mm.

In 0°/90°, RVE model comprises two layers having voids in mutually perpendicular directions. Thus, 0°/90° RVE model exhibited transversely isotropic characteristics as expected with the similar elastic constants in two perpendiculars (longitudinal and transverse) directions in all layer thickness. The comparison of elastic constants in the two orientations is shown in Fig. 13. The Young's modulus along the first and second axis reduced by 8% with an increase in layer height from 0.1 to 0.4 mm, and along the third axis, the percentage reduction of Young's modulus remained same as that in 0° raster oriented component. Shear modulus showed a decrease of 8% for G_{12} and 19% for G_{13} and G_{23} with an increase in the layer height. The effective elastic constants estimated by analysis of cross section-based RVE model are shown in Table 7. The microscale characteristics observed from microscale RVE analysis assumed as homogenised effective elastic constants in the FDM structure. FDM structure's effective elastic property dependence on raster angles and layer thickness are predictable based on microanalysis RVE model resembling the actual cross section.

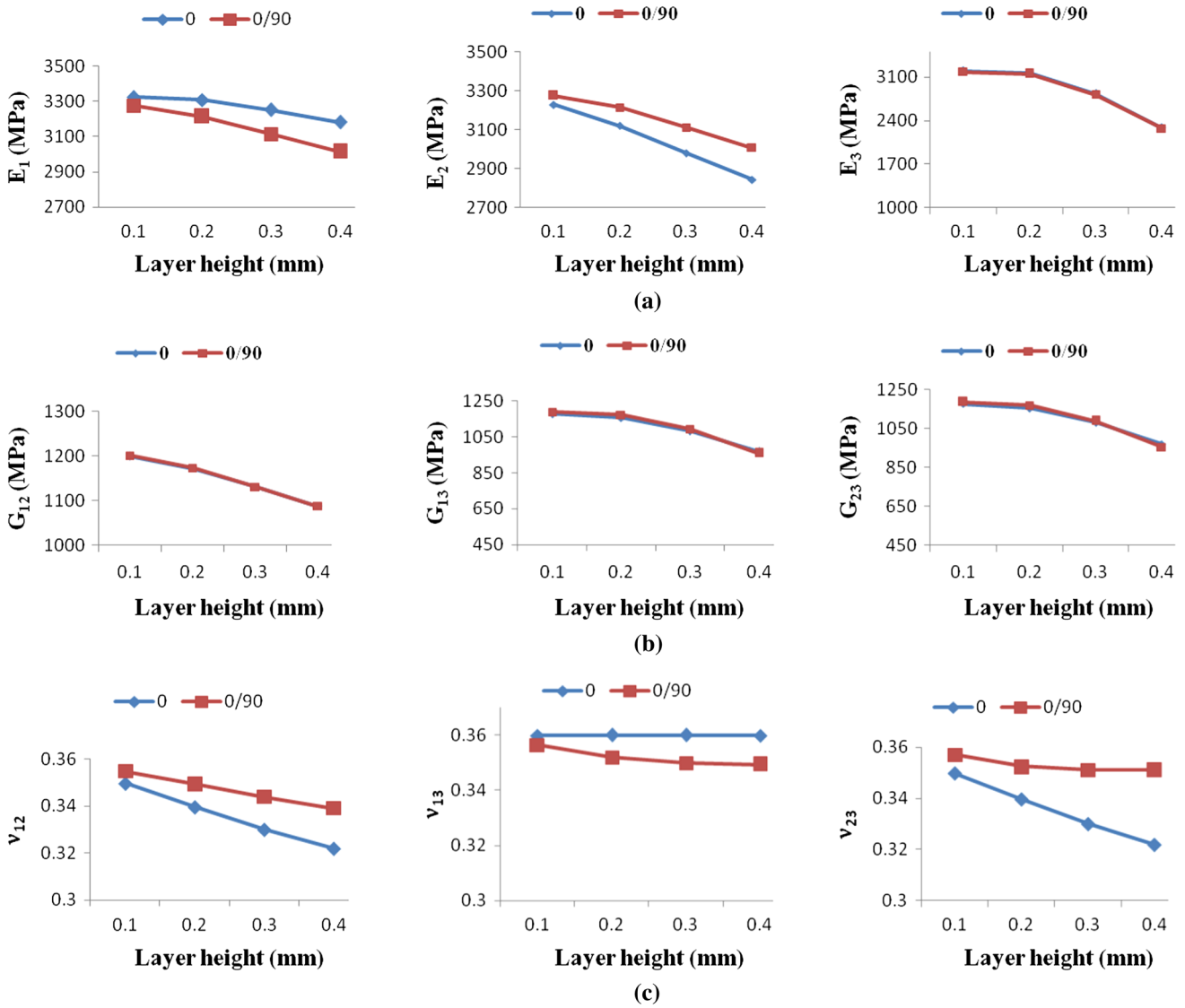

Fig. 13 **a** Variation of elasticity modulus E_1, E_2 and E_3 with layer height, **b** variation of shear modulus G_{12}, G_{13} and G_{23} with layer height and **c** variation of Poisson's ratio ν_{12}, ν_{13} and ν_{23} with layer height

Table 7 Effective elastic constants estimated by analysis of cross section-based RVE model

Elastic constants	0°				0°/90°			
	Layer height (mm)				Layer height (mm)			
	0.10	0.20	0.30	0.40	0.10	0.20	0.30	0.40
E_1 (MPa)	3324.37	3309.08	3251.64	3182.35	3276.67	3215.02	3116.21	3014.69
E_2 (MPa)	3228.86	3120.70	2979.64	2844.13	3276.41	3214.37	3112.08	3008.39
E_3 (MPa)	3198.60	3156.07	2830.29	2281.74	3185.63	3150.93	2818.96	2272.47
G_{12} (MPa)	1199.90	1172.60	1131.10	1087.60	1200.90	1173.40	1131.40	1087.60
G_{13} (MPa)	1192.00	1181.30	1095.60	941.14	1186.50	1170.10	1089.60	955.92
G_{23} (MPa)	1178.40	1156.90	1082.30	970.35	1187.90	1171.70	1092.90	959.45
ν_{12}	0.35	0.34	0.33	0.32	0.35	0.35	0.34	0.34
ν_{13}	0.36	0.36	0.36	0.36	0.36	0.35	0.35	0.35
ν_{23}	0.35	0.34	0.34	0.34	0.36	0.35	0.35	0.35

4 Conclusion

The morphology of the FDM prints revealed the presence of a periodic array of voids. The presence of these voids causes directional behaviour in FDM structures. Thus, the directional properties of the FDM components need to be estimated for designing the functional components. The microscale model capturing the material disparity can address directional response. Microscale RVE models of FDM structures in different orientations capturing the void features of the actual cross section were created and analysed for determining the directional properties based on the volume average method. RVE with 0° raster orientation exhibited orthotropic characteristics, whereas RVE with 0°/90° raster orientation exhibited transversely isotropic characteristics. With lower layer height, the elasticity moduli approach isotropic behaviour. The elasticity modulus along the direction of raster orientation exhibited the highest value, and that along vertical direction showed the lowest value among the three axes. The Young's modulus along the vertical direction exhibited the maximum percentage deviation within the printable levels of layer height. The constitutive matrix derived from the RVE model with 0° raster orientation can be transformed to determine properties of FDM-printed components in any raster angle. Hence, the effect of process parameters on directional properties can be determined from the numerical analysis of microscale RVE based on the actual cross section of the FDM print.

The elastic properties obtained from the numerical analysis of microscale RVE can be homogenised for the region printed with same parameters. The homogenised properties thus determined based on the actual cross-sectional geometry provide the appropriate material data for numerical simulation of the functional FDM components. This homogenisation technique can be extended further to study the mechanical, electrical and thermal characteristics of FDM components printed using composite polymer filaments with different volume fractions of constituents.

References

1. Ngo TD, Kashani A, Imbalzano G, Nguyen KTQ, Hui D (2018) Additive manufacturing (3D printing): a review of materials, methods, applications and challenges. Compos B 143:172–196. https://doi.org/10.1016/j.compositesb.2018.02.012
2. Oropallo W, Piegl LA (2016) Ten challenges in 3D printing. Eng Comput 32:135–148. https://doi.org/10.1007/s00366-015-0407-0
3. Ning F, Cong W, Hu Z, Huang K (2017) Additive manufacturing of thermoplastic matrix composites using fused deposition modeling: a comparison of two reinforcements. J Compos Mater 51:3733–3742. https://doi.org/10.1177/0021998317692659
4. Yang C, Wang B, Li D, Tian X (2017) Modelling and characterisation for the responsive performance of CF/PLA and CF/PEEK smart materials fabricated by 4D printing. Virtual Phys Prototyp 12:69–76. https://doi.org/10.1080/17452759.2016.1265992
5. Singh R, Ranjan N (2018) Experimental investigations for preparation of biocompatible feedstock filament of fused deposition modeling (FDM) using twin screw extrusion process. J Thermoplast Compos Mater 31:1455–1469. https://doi.org/10.1177/0892705717738297
6. Mohan N, Senthil P, Vinodh S, Jayanth N (2017) A review on composite materials and process parameters optimisation for the fused deposition modelling process. Virtual Phys Prototyp 2759:47–59. https://doi.org/10.1080/17452759.2016.1274490
7. Kumar S, Kurth J-P (2010) Composites by rapid prototyping technology. Mater Des 31:850–856. https://doi.org/10.1016/j.matdes.2009.07.045
8. Levenhagen NP, Dadmun MD (2018) Interlayer diffusion of surface segregating additives to improve the isotropy of fused deposition modeling products. Polymer 152:35–41. https://doi.org/10.1016/j.polymer.2018.01.031
9. Boparai K, Singh R, Singh H (2015) Comparison of tribological behaviour for Nylon6-Al-Al_2O_3 and ABS parts fabricated by fused deposition modelling. Virtual Phys Prototyp 10:59–66. https://doi.org/10.1080/17452759.2015.1037402
10. Yamamoto BE, Trimble AZ, Minei B, Ghasemi Nejhad MN (2019) Development of multifunctional nanocomposites with 3-D printing additive manufacturing and low graphene loading. J Thermoplast Compos Mater 32:383–408. https://doi.org/10.1177/0892705718759390
11. Kaynak C, Varsavas SD (2018) Performance comparison of the 3D-printed and injection-molded PLA and its elastomer blend and fiber composites. J Thermoplast Compos Mater 32:501–520. https://doi.org/10.1177/0892705718772867

12. Ilardo R, Williams CB (2010) Design and manufacture of a Formula SAE intake system using fused deposition modeling and fiber reinforced composite materials. Rapid Prototyp J 16:174–179. https://doi.org/10.1108/13552541011034834
13. Prada JG, Cazon A, Carda J, Aseguinolaza A (2016) Direct digital manufacturing of an accelerator pedal for a formula student racing car. Rapid Prototyp J 22:311–321. https://doi.org/10.1108/RPJ-05-2014-0065
14. Klippstein H, Diaz A, Sanchez DC, Hassanin H, Zweiri Y (2017) Fused deposition modeling for unmanned aerial vehicles (UAVs): a review. Adv Eng Mater 20:1–17. https://doi.org/10.1002/adem.201700552
15. Cazón A, Prada JG, García E, Larraona GS, Ausejo S (2015) Pilot study describing the design process of an oil sump for a competition vehicle by combining additive manufacturing and carbon fibre layers. Virtual Phys Prototyp 10:149–162. https://doi.org/10.1080/17452759.2015.1076240
16. Javaid M, Haleem A (2018) Additive manufacturing applications in medical cases: a literature based review. Alex J Med 54:411–422. https://doi.org/10.1016/j.ajme.2017.09.003
17. Jain P, Kuthe AM (2013) Feasibility Study of manufacturing using rapid prototyping: FDM Approach. Procedia Eng 63:4–11. https://doi.org/10.1016/j.proeng.2013.08.275
18. Singh R, Singh S (2014) Development of nylon based FDM filament for rapid tooling application. J Inst Eng India Ser C 95:103–108. https://doi.org/10.1007/s40032-014-0108-2
19. Sunpreet S, Rupinder S (2016) Fused deposition modelling based rapid patterns for investment casting applications: a review. Rapid Prototyp J 22:123–143. https://doi.org/10.1108/RPJ-02-2014-0017
20. Jayanth N, Senthil P (2019) Application of 3D printed ABS based conductive carbon black composite sensor in void fraction measurement. Compos B 159:224–230. https://doi.org/10.1016/j.compositesb.2018.09.097
21. Isakov DV, Lei Q, Castles F, Stevens CJ, Grovenor CRM, Grant PS (2016) 3D printed anisotropic dielectric composite with meta-material features. Mater Des 93:423–430. https://doi.org/10.1016/j.matdes.2015.12.176
22. Gardner JM, Sauti G, Kim J, Cano RJ, Wincheski RA, Stelter CJ, Grimsley BW, Working DC, Siochi EJ (2016) 3-D printing of multifunctional carbon nanotube yarn reinforced components. Addit Manuf 12:38–44. https://doi.org/10.1016/j.addma.2016.06.008
23. Schmitz DP, Ecco LG, Dul S, Pereira ECL, Soares BG, Barra GMO, Pegoretti A (2018) Electromagnetic interference shielding effectiveness of ABS carbon-based composites manufactured via fused deposition modelling. Mater Today Commun 15:70–80. https://doi.org/10.1016/j.mtcomm.2018.02.034
24. Huang B, Singamneni S (2015) Raster angle mechanics in fused deposition modelling. J Compos Mater 49:363–383. https://doi.org/10.1177/0021998313519153
25. Dizon JRC, Espera AH Jr, Chen Q, Advincula RC (2018) Review: mechanical characterization of 3D-printed polymers. Addit Manuf. https://doi.org/10.1016/j.addma.2017.12.002
26. Ahn SH, Montero M, Odell D, Roundy S, Wright PK (2002) Anisotropic material properties of fused deposition modeling ABS. Rapid Prototyp J 8:248–257. https://doi.org/10.1108/13552540210441166
27. Sood AK, Ohdar RK, Mahapatra SS (2010) Parametric appraisal of mechanical property of fused deposition modelling processed parts. Mater Des 31:287–295. https://doi.org/10.1016/j.matdes.2009.06.016
28. Croccolo D, De Agostinis M, Olmi G (2013) Experimental characterization and analytical modelling of the mechanical behaviour of fused deposition processed parts made of ABS-M30. Comput Mater Sci 79:506–518. https://doi.org/10.1016/j.commatsci.2013.06.041
29. Dawoud M, Taha I, Ebeid SJ (2016) Mechanical behaviour of ABS: an experimental study using FDM and injection moulding techniques. J Manuf Process. https://doi.org/10.1016/j.jmapro.2015.11.002
30. Ziemian S, Okwara M, Ziemian CW (2015) Tensile and fatigue behavior of layered acrylonitrile butadiene styrene. Rapid Prototyp J 21:270–278. https://doi.org/10.1108/rpj-09-2013-0086
31. Abbott AC, Tandon GP, Bradford RL, Koerner H, Baur JW (2018) Process-structure-property effects on ABS bond strength in fused filament fabrication. Addit Manuf 19:29–38. https://doi.org/10.1016/j.addma.2017.11.002
32. Mcilroy C, Olmsted PD (2017) Disentanglement effects on welding behaviour of polymer melts during the fused-filament-fabrication method for additive manufacturing. Polymer 123:376–391. https://doi.org/10.1016/j.polymer.2017.06.051
33. Ravindrababu S, Govdeli Y, Wong ZW, Kayacan E (2018) Evaluation of the influence of build and print orientations of unmanned aerial vehicle parts fabricated using fused deposition modeling process. J Manuf Process 34:659–666. https://doi.org/10.1016/j.jmapro.2018.07.007
34. Motaparti KP, Taylor G, Leu MC, Chandrashekhara K, Castle J, Matlack M (2017) Experimental investigation of effects of build parameters on flexural properties in fused deposition modelling parts. Virtual Phys Prototyp 12:207–220. https://doi.org/10.1080/17452759.2017.1314117
35. Jiang S, Liao G, Xu D, Liu F, Li W, Cheng Y, Li Z, Xu G (2019) Mechanical properties analysis of polyetherimide parts fabricated by fused deposition modeling. High Perform Polym 31:97–106. https://doi.org/10.1177/0954008317752822
36. Wang L, Gardner DJ (2017) Effect of fused layer modeling (FLM) processing parameters on impact strength of cellular polypropylene. Polymer 113:74–80. https://doi.org/10.1016/j.polymer.2017.02.055
37. Chacón JM, Caminero MA, García-Plaza E, Núñez PJ (2017) Additive manufacturing of PLA structures using fused deposition modelling: Effect of process parameters on mechanical properties and their optimal selection. Mater Des 124:143–157. https://doi.org/10.1016/j.matdes.2017.03.065
38. Rajpurohit SR, Dave HK (2018) Effect of process parameters on tensile strength of FDM printed PLA part. Rapid Prototyp J 24:1317–1324. https://doi.org/10.1108/RPJ-06-2017-0134
39. Lanzotti A, Grasso M, Staiano G, Martorelli M (2015) The impact of process parameters on mechanical properties of parts fabricated in PLA with an open-source 3-D printer. Rapid Prototyp J 21:604–617. https://doi.org/10.1108/rpj-09-2014-0135
40. Tymrak BM, Kreiger M, Pearce JM (2014) Mechanical properties of components fabricated with open-source 3-D printers under realistic environmental conditions. Mater Des 58:242–246. https://doi.org/10.1016/j.matdes.2014.02.038
41. Bhalodi D, Zalavadiya K, Gurrala PK (2019) Influence of temperature on polymer parts manufactured by fused deposition modeling process. J Braz Soc Mech Sci Eng 41:1–11. https://doi.org/10.1007/s40430-019-1616-z
42. Casavola C, Cazzato A, Moramarco V, Pappalettere C (2016) Orthotropic mechanical properties of fused deposition modelling parts described by classical laminate theory. Mater Des 90:453–458. https://doi.org/10.1016/j.matdes.2015.11.009
43. Liu X, Shapiro V (2016) Homogenization of material properties in additively manufactured structures. Comput Aided Des 78:71–82. https://doi.org/10.1016/j.cad.2016.05.017
44. Domingo-Espin M, Puigoriol-Forcada JM, Garcia-Granada A-A, Llumà J, Borros S, Reyes G (2015) Mechanical property characterization and simulation of fused deposition modeling Polycarbonate parts. Mater Des 83:670–677. https://doi.org/10.1016/j.matdes.2015.06.074

45. Rodriguez JF, Thomas JP, Renaud JE (2000) Characterization of the mesostructure of styrene materials. Rapid Prototyp J 6:175–186. https://doi.org/10.1108/13552540010337056
46. Magalhães LC, Volpato N, Luersen MA (2014) Evaluation of stiffness and strength in fused deposition sandwich specimens. J Braz Soc Mech Sci Eng 36:449–459. https://doi.org/10.1007/s40430-013-0111-1
47. Guessasma S, Belhabib S, Nouri H (2015) Significance of pore percolation to drive anisotropic effects of 3D printed polymers revealed with X-ray μ-tomography and fi nite element computation. Polymer 81:29–36. https://doi.org/10.1016/j.polymer.2015.10.041
48. Rodríguez JF, Thomas JP, Renaud JE (2003) Mechanical behavior of acrylonitrile butadiene styrene fused deposition materials modeling. Rapid Prototyp J 9:219–230. https://doi.org/10.1108/13552540310489604
49. Omairey SL, Dunning PD, Sriramula S (2018) Development of an ABAQUS plugin tool for periodic RVE homogenisation. Eng Comput 35:1–11. https://doi.org/10.1007/s00366-018-0616-4
50. Calneryte D, Barauskas R, Milasiene D, Maskeliunas R, Neciunas A, Ostreika A, Patasius M, Krisciunas A (2018) Multi-scale finite element modeling of 3D printed structures subjected to mechanical loads. Rapid Prototyp J 24:177–187. https://doi.org/10.1108/RPJ-05-2016-0074
51. Somireddy M, Czekanski A, Singh CV (2018) Development of constitutive material model of 3D printed structure via FDM. Mater Today Commun 15:143–152. https://doi.org/10.1016/j.mtcomm.2018.03.004
52. Barbero EJ (2011) Finite element analysis of composite materials. CRC Press, Boca Raton